



Measurement report: Ice nucleation ability of perthite feldspar powder

Julia Canet^{1,2}, Laura Rodríguez¹, Galit Renzer⁴, Pura Alfonso⁶, Mischa Bonn⁴, Konrad Meister^{4,5}, Maite Garcia-Valles³, Albert Verdaguer^{1*}

- ¹Institut de Ciència de Materials de Barcelona ICMAB-CSIC, Campus Universitat Autònoma de Barcelona (UAB), 08193 Bellaterra, Spain.
 - ²Department of Chemical Engineering and Materials Science, Institut Químic de Sarrià, Universitat Ramon Llull, Via Augusta 390, 08017 Barcelona, Spain
 - ³Departament de Mineralogia, Petrologia i Geologia Aplicada, Universitat de Barcelona (UB), Barcelona, Spain
- 4Department of Molecular Spectroscopy, Max Planck Institute for Polymer Research, Mainz 55128, Germany
 - ⁵Department of Chemistry and Biochemistry, Boise State University, Boise, Idaho 83725, USA
 - ⁶Departament d'Enginyeria Minera, Industrial i TIC, Universitat Politècnica de Catalunya (UPC), Manresa, Spain.

Correspondence to: Albert Verdaguer (averdaguer@icmab.es)

Abstract. Feldspars are among the most efficient mineral ice-nucleating particles (INPs) in the atmosphere. However, their nucleation behavior varies significantly across natural samples. This study investigates six feldspar powders selected for their perthitic or anti-perthitic textures and spanning a range of K/Na compositions. All samples were comprehensively characterized in terms of mineralogy, bulk and surface chemistry, and microstructure. Droplet freezing assays revealed consistent onset temperatures between -2 and -4 °C, suggesting the presence of shared active nucleation sites across all feldspar types. Cumulative and differential freezing spectra revealed marked differences in the density and distribution of icenucleating sites, which were found to correlate with both feldspar composition and microtexture. Using HUB analysis, different subpopulations of ice-nucleating sites were identified. Perthites showing microcline structures exhibited a continuous increase in nucleation site density with decreasing temperature as subpopulations became active. In contrast, samples lacking dominant microcline structures showed plateaus in the cumulative spectra within specific temperature ranges, indicating a significant reduction in certain subpopulations. These findings highlight the crucial role of exsolution textures and crystallographic structure in regulating feldspar ice-nucleation efficiency. The results have implications for understanding feldspar behavior in the atmosphere and for improving predictive models in cloud microphysics.

1 Introduction

15

The formation of ice crystals in clouds plays a critical role in Earth's hydrological cycle and climate system, as it influences cloud radiative properties, initiates precipitation, and determines cloud lifetime (Burrows et al., 2022; Knopf & Alpert, 2023; B. J. Murray et al., 2012, 2021). In the atmosphere, pure water droplets can supercool to temperatures as low as -38 °C before undergoing homogeneous ice nucleation (homogeneous IN). However, most natural clouds are mixed-phase, containing both supercooled liquid droplets and ice crystals. In such clouds, ice formation typically occurs at much higher temperatures through



55



heterogeneous IN, which is triggered by airborne particles collectively known as ice-nucleating particles (INPs). A detailed understanding of INPs and their role in cloud microphysics is crucial for enhancing the accuracy of climate models (Burrows et al., 2022), which are vital tools for forecasting climate change and developing mitigation strategies.

Among known INPs, mineral dust is widely recognized as one of the most influential contributors to heterogeneous IN in the atmosphere (Cziczo et al., 2013; Hoose & Möhler, 2012). These particles are emitted in large quantities through the weathering of rocks and subsequent wind transport, making them a globally abundant source of INPs. More than a decade ago, feldspars, aluminosilicate minerals commonly found in terrestrial dust, were identified as particularly potent INPs, capable of initiating ice formation at significantly warmer temperatures than most other minerals (Atkinson et al., 2013). Since then, considerable research has focused on elucidating the mechanisms that govern ice-nucleating efficiency of feldspars (Harrison et al., 2016; Kanji et al., 2017; A. Kiselev et al., 2016; A. A. Kiselev et al., 2021; Welti et al., 2019; Whale et al., 2017).

Studies have shown that ice crystals preferentially grow on specific crystallographic faces of feldspar (A. Kiselev et al., 2016), and that the defects (Friddle & Thürmer, 2019; A. A. Kiselev et al., 2021; Liang et al., 2024) and surface porosity (Pach & Verdaguer, 2019) can significantly enhance nucleation efficiency at those sites. However, feldspars exhibit a wide range of IN efficiencies. Samples with similar bulk composition can initiate freezing at vastly different temperatures—ranging from approximately -3 to -20 °C (Kanji et al., 2017; Whale et al., 2017). Graphs comparing the IN properties of different feldspars reveal not only significant variation in the onset temperature of freezing, but also in the shape of the freezing efficiency curves—commonly referred to as freezing spectra (Kanji et al., 2017). While all spectra generally show increased IN efficiency at lower temperatures, the diverse curve shapes make direct comparisons difficult and their interpretation often complex. This variability is primarily attributed to the fact that IN becomes thermodynamically favorable only when a critical ice embryo reaches nanometer-scale dimensions. Consequently, nanoscale surface properties—especially at active sites—are crucial in determining the freezing behavior of feldspars.

As discussed in the literature, features such as crystal defects, surface roughness, porosity, phase boundaries, and other microto nanoscale heterogeneities can significantly affect the IN activity of feldspars (Friddle & Thürmer, 2019; Pach & Verdaguer, 2019). However, these features are difficult to control, quantify, or fully characterize. As a result, predicting the IN potential of a feldspar sample solely based on its bulk chemical or mineralogical composition remains a challenge. Nonetheless, it is well established that feldspars with specific crystal structures and chemical compositions tend to exhibit consistently higher nucleation activity. This suggests that nanoscale properties responsible for enhanced IN may not be entirely independent of macroscopic structural characteristics.

Feldspars include a group of minerals from the tectosilicates subclass that are among the most abundant minerals on the Earth's surface. Among the main rock-forming minerals are orthoclase (Or), microcline (Mc), albite (Ab), and the plagioclase (Pl) solid-solution series. Their general formula is $X(Si, Al)Si_2O_8$, where X typically represents potassium (K), sodium (Na), and calcium (Ca). K-feldspars, (KAlSi₃O₈), crystallize into three polymorphs: Mc, which is triclinic, with aluminum (Al) and silicon (Si) fully ordered in the structure; Or, monoclinic, is partially ordered, and sanidine (Sa), also monoclinic, with Al and Si distribution fully disordered. The latter forms only at high temperatures and is mainly found in acidic volcanic rocks.





Feldspars constitute a ternary partial solid solution of: orthoclase KAlSi₃O₈, albite KAlSi₃O₈, and anorthite (An) CaAl₂Si₂O₈ (Fig. 1a). The Ab-An series constitutes a complete solid solution named Pl.

The Or-Ab solid solution is fully miscible only at high temperatures. With a decrease in temperature, alkali feldspars unmix, giving rise to an intergrowth of Or- and Ab-rich phases. This immiscibility is produced by the relatively high difference in size between the Na and K atomic radius. One well-known texture is the perthite, which consists of fine, unsolved albite (Na-rich) lamellae within a Mc or Or (K-rich) host crystal. These lamellae typically align with the (100) crystallographic plane and are especially prominent in monoclinic feldspars. The anti-perthite structure, in contrast, features K-rich feldspar lamellae exsolved within a Na-rich albite matrix.

Fig. 1a illustrates the relationship between the molar composition of these intergrowths and the resulting exsolution textures, underscoring the influence of chemical composition on the structural and textural evolution of feldspar minerals during thermal history. Triclinic K-feldspar, or Mc, can form twinning following two perpendicular twin laws, known as the Albite law and the Periclase law, which give rise to the so-called tartan twin.

K-feldspars—particularly Mc—have consistently been identified as the most efficient ice nucleators (Augustin-Bauditz et al., 2014), while Ab has also shown variable but sometimes significant activity (Welti et al., 2019). In contrast, Pl-feldspars generally exhibit much lower IN efficiency. Given that alkali feldspars exhibit the highest efficiency in initiating IN at relatively high temperatures, they are especially relevant to mixed-phase cloud formation. Among them, perthitic and antiperthitic feldspars are of particular interest, as their exsolution textures introduce nanoscale heterogeneities that are likely to influence the formation and distribution of active nucleation sites, with activity at temperatures above —5 °C.

Despite this importance, previous studies have reported highly variable freezing spectra for alkali feldspars, even within perthitic samples. Such discrepancies likely arise from uncontrolled differences in sample provenance, crystallographic structure, and microstructural features. To address this, we systematically investigate feldspars with perthitic and anti-perthitic textures collected from two well-characterized mining sites. By combining precise mineralogical and microstructural characterization with quantitative freezing assays, our study aims to disentangle the influence of chemical composition and texture on ice-nucleating efficiency. This controlled approach provides more reproducible insight into the mechanisms by which alkali feldspar structure governs atmospheric ice nucleation, thereby narrowing the gap between mineralogical properties and their climatic relevance.

2 Experimental

2.1 Materials

Six different feldspar minerals, sourced from two industrial quarries, were investigated for their IN activity. Two K-rich feldspars were sourced directly from the French industrial minerals company Imerys, collected from different extraction fronts. These samples are referred to as ImerysK1 (IK1) and ImerysK2 (IK2). Although the company did not disclose specific mine locations, the samples are known to originate from active industrial operations. Four additional samples were obtained from



100

105

120

125



LLANSÀ, S.A. Company, a feldspar quarry located in Llançà, Catalonia, Spain. These included two samples with predominantly Na-rich feldspars and two with a roughly balanced K/Na composition, depending on the extraction front. Photographs of the extraction fronts are shown in Fig. S1 of the supplementary material. The samples were labeled LlançaNa1 (LNa1), LlançaNa2 (LNa2), LlançaNaK1 (LNaK1), and LlançaNaK2 (LNaK2); see Fig. 1b and Table 1 for the full list and classification of the feldspar minerals used. The bulk rocks were processed in two steps. First, portions of each were crushed and homogenized via ball milling to produce fine powders, primarily for ice nucleation experiments and also for granulometric, chemical, and mineralogical analysis. Second, unprocessed fragments were cut and polished to prepare thin sections and mounts for petrographic and microstructural characterization. This dual approach enabled correlation of ice nucleation behavior with crystallographic texture and surface features of the parent minerals. Ultrapure water (resistivity 18 MΩ cm), dispensed from a Milli-Q purification system, was used in all experiments.

2.2 Chemical and mineral composition

The chemical composition of the feldspar samples was determined using a Philips PW 2400 X-ray fluorescence (XRF) sequential spectrometer located at the Centres Científics i Tecnològics de la Universitat de Barcelona (CCiT-UB). Major oxides (expressed as weight percent) were quantified via the fused bead method, while trace elements (in ppm) were measured using pressed powder pellets (See Table 1 and Tables S1 and S2 in the supplementary material). Quantification was calibrated against certified geological standards to ensure analytical accuracy. In addition, thermal treatments were conducted to assess Loss on Ignition [ASTM D7348-21].

Mineralogical characterization was conducted through a combination of X-ray diffraction (XRD), optical, and Scanning Electron Microscopy (SEM). XRD measurements were performed on a PANalytical X'Pert System diffractometer, configured in Bragg-Brentano geometry with Cu K α radiation ($\lambda = 1.54061$ Å). Phase identification and semi-quantitative analysis were conducted with the XPert Graphics Identify software (Philips). For microstructural and petrographic examination, double-polished thin sections were observed using a Nikon ACT-1 optical microscope (see Fig. S2 at the supplementary material). The same sections were examined using a Hitachi TM-1000 tabletop SEM, coupled with energy-dispersive X-ray spectroscopy (EDS) to analyze microstructural features and verify elemental composition.

2.3 Particle size distribution and specific surface area of feldspar powder

Particle-size distribution (PSD) of the ground feldspar powders was measured by laser diffraction using a Mastersizer 2000 analyzer and its Hydro 2000SM accessory. Feldspar powders were dispersed in deionized water, and the suspensions were sonicated for at least 5 min prior to measurement to avoid particle segregation. The specific surface area (S_a) was determined



135



by N_2 adsorption/desorption at 77 K using an ASAP 2020 (Micromeritics Inc.). Prior to measurements, feldspar powders were degassed at 393 K for 24 h. S_a was calculated by applying the BET method (*Brunauer et al.*, 1938).

2.4 Water freezing Ice nucleation measurements

The behavior of the investigated IN samples was assessed using the immersion freezing method, which evaluates the temperature at which aqueous droplets containing suspended mineral particles freeze. Feldspar suspensions were serially diluted in ultrapure water using an automated liquid handling station (epMotion ep5073, Eppendorf, Hamburg, Germany) to obtain concentrations of 10, 5, 2, 1, 0.5, 0.1, 0.05, 0.01 and 0.001 wt%. For each dilution, 96 droplets of 3 µL were dispensed into two 384-well plates, which were subsequently subjected to ice nucleation experiments using the high-throughput Twin-plate Ice Nucleation Assay (TINA), which has been described in detail elsewhere (Kunert et al., 2018)(19).

The plates were subjected to a controlled cooling regime from 0 to -30 °C at a rate of 1 °C min⁻¹. Droplet freezing was monitored using two infrared cameras (Seek Thermal Compact XR, Seek Thermal Inc., USA), providing a temperature resolution of \pm 0.2 °C. From the resulting data, the fraction of frozen droplets, $f_{ice}(T)$, was calculated as a function of temperature. Cumulative freezing spectra were obtained from $f_{ice}(T)$ using the approach proposed by Vali (Vali, 1971, 2014, 2019) with normalization per gram of mineral. Each experiment was performed in triplicate on independent sample batches. Control measurements using pure water showed a background freezing point near -21 °C. At concentrations < 0.001 wt%, the freezing behavior converged with that of ultrapure water (-21 °C) and therefore did not provide additional information on the influence of feldspar INPs. For this reason, suspensions below this threshold were omitted from the quantitative analysis, which was restricted to data above -20 °C.





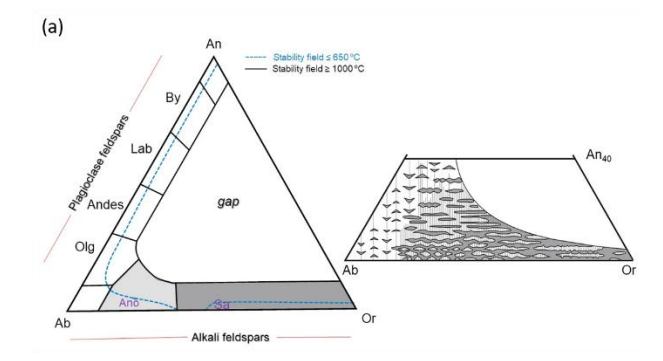
3. Results

150

155

3.1 Mineralogical and chemical characterization

The mineralogical composition of the feldspar samples was analyzed using powder XRD, enabling a semi-quantitative assessment of the mineral phases present. The main minerals determined are Na-feldspar, K-feldspar, and quartz, and a secondary phase is muscovite (KAl(Si₃Al)O₁₀(OH, F)₂), a mica-type mineral. XRD data indicate that all feldspar samples from the LLANSÀ S.A. mine (LNa1, LNa2, LNaK1, and LNaK2) are richer in Na-feldspar (Ab) than in K-feldspar (Mc or Or). The LNaK samples exhibit a more balanced distribution between the two phases. Quartz and minor muscovite are also detected in these samples. In contrast, the Imerys samples (IK1 and IK2) are rich in K-feldspar, with only minor Na-feldspar presence. Neither quartz nor muscovite is identified in these latter samples. Semi-quantitative abundances of these mineral phases, expressed as weight percentages, are shown in Fig. 1b.



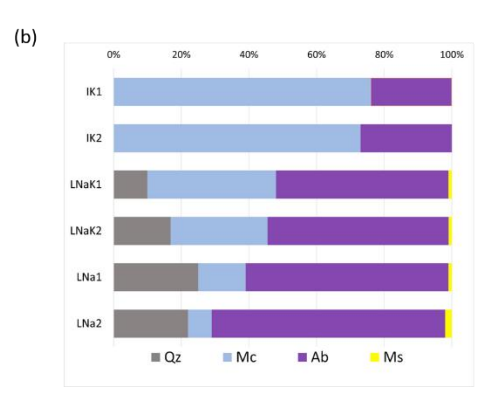


Figure 1. a) Ternary feldspar diagram defined by the endmembers orthoclase (Or) KAlSi₃O₈, albite (Ab) NaAlSi₃O₈, and anorthite (An) CaAl₂Si₂O₈. Compositions along the Or–Ab join correspond to alkali feldspars, whereas those along the Ab–An join define the plagioclase (Pl) series. The schematic inset illustrates perthitic and anti-perthitic intergrowths of alkali feldspars and their approximate position within the ternary compositional space. b) Semi-quantitative mineralogical composition (wt.%) of microcline (Mc), albite (Ab), and muscovite (Ms) for each feldspar as obtained by XRD.



175

185

190

195



Table 1. Bulk chemical composition of the studied feldspars, expressed as wt% oxides determined by XRF. Oxide ratios $(K_2O/Na_2O \text{ and }SiO_2O/Al_2O_3)$ and Loss on ignition (LOI) are also reported.

Samples	SiO ₂	Al ₂ O ₃	Na ₂ O	K ₂ O	CaO	K ₂ O/Na ₂ O	SiO ₂ /Al ₂ O ₃	LOI
IK1	65.0	18.8	2.9	12.8	0.3	4.3	3.4	_
IK2	65.8	18.8	3.3	11.9	0.1	3.6	3.5	0.2
LNaK1	75.2	14.8	3.7	3.8	0.8	1.0	5.1	0.8
LNaK2	73.2	15.3	5.1	4.8	0.7	0.9	4.8	0.4
LNa1	75.7	14.2	5.9	2.3	0.7	0.4	5.3	0.3
LNa2	75.7	14.5	6.8	1.4	0.8	0.2	5.2	0.4

XRF analysis (Table 1) reveals that IK1 and IK2 contain more than 10 wt% K₂O and exhibit K₂O/Na₂O ratios between 3 and 5, consistent with a K-rich feldspar classification. In contrast, LNa1 and LNa2 are Na-rich, with Na₂O contents exceeding 5 wt% and K₂O/Na₂O ratios well below 1. LNaK1 and LNaK2 show intermediate alkali compositions, with K₂O/Na₂O ratios close to unity. Minor oxides (< 0.5 wt%) are reported in Table S1 at the supplementary material, together with full oxide compositions as in Table 1. LOI values are also reported to account for adsorbed water and volatiles, which are found to be negligible. Notably, the Si/Al ratio in the Llançà samples is ~5, while in the Imerys samples it is closer to 3.5, suggesting greater silica enrichment in the former and relatively higher Al₂O₃ content in the latter. The absence of mica phases in the Imerys samples implies that Al is incorporated into the feldspar structure via Si–Al substitution, with charge compensation provided by elevated K⁺ content.

The K/Na distribution in selected samples was further investigated through SEM analysis of metallographically polished feldspar surfaces. SEM imaging was performed on three samples exhibiting a wide range of K/Na ratios—IK1, LNa2, and LNaK2—as shown in Fig. 2b. The mineralogy identified via SEM corroborates previous results obtained from XRD. All examined samples exhibit characteristic exsolution textures between the two alkali feldspar phases.

SEM observations of samples IK1 and LNaK2 (Fig. 2a) reveal a typical perthitic texture, where K-feldspar—identified as Mc (brighter regions due to its higher average atomic number, $Z \approx 18$)—hosts elongated intergrowths of Ab-type sodic plagioclase (darker regions, $Z \approx 11$). In the LNaK2 sample, small apatite crystals [Ca₅(PO₄)₃(OH, Cl, F,)] are also observed as solid inclusions. In contrast, the LNa1 sample (Fig. 2a) shows an anti-perthitic texture, where Ab forms the dominant matrix with fine exsolutions of K-feldspar (Mc). Apatite inclusions are again present. All samples exhibit aligned porosity and dark-contrast features associated with fluid inclusions, indicating a shared history of hydrothermal alteration or mineral-fluid interactions.

Fig. 2b shows the XRD spectra for each of the studied samples in the 2θ range of $28 - 32^{\circ}$, where characteristic peaks associated with Mc, Or, and Ab structures can be clearly identified (the full-range spectra are also provided in Fig. S3 of the supplementary material). Sharp peaks corresponding to Mc and Ab are clearly visible in the spectra of the IK samples from Imerys. In contrast, the samples from Llançà, which are richer in sodium, show well-defined Ab peaks but significantly less pronounced Mc peaks. These peaks exhibit lower intensity and considerable broadening, particularly in the LNa samples,





where Mc reflections nearly disappear. These observations suggest that the dominant K-feldspar phase in the Llançà samples is more disordered, likely tending toward Or rather than the well-ordered Mc.

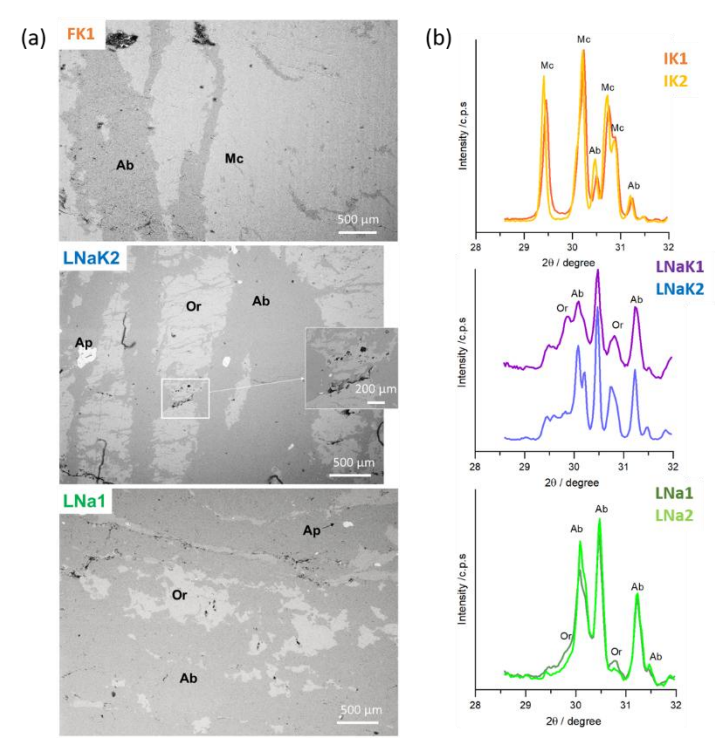


Figure 2. a) SEM images of polished surfaces of feldspar samples: IK1, LNaK2, and LNa1. Mineral phases are labeled as: orthoclase (Or), K-feldspar; albite (Ab), Na-feldspar; and apatite (Ap), Ca-phosphate. In agreement with the mineralogical analyses shown in Fig. 1 and 2, IK1 and LNaK2 display perthitic textures, whereas LNa1 exhibits an anti-perthitic texture. b) The corresponding XRD plots in the 2θ range of 28 – 32°. Peaks corresponding to Ab are observed in all samples, while microcline (Mc) peaks are observed only in IK1 and IK2.

3.2 Powder size and specific area

Particle size characterization was performed using laser diffraction, and the key metrics—D10, D50, D90, and average particle size—are presented in Table 2. D10, D50, and D90 values represent the diameters below which 10%, 50%, and 90% of the particles fall, respectively. Complementary surface area measurements were conducted using the BET method. These analyses revealed surface area variations of up to a factor of four across the samples, ranging from 1.35 m² g⁻¹ for LNaK1 (the lowest) to 5.29 m² g⁻¹ for LNaK2 (the highest). For the LNa2 sample, two distinct powders were provided, each produced from the same bulk material but subjected to different milling durations, resulting in varying particle size distributions.



225

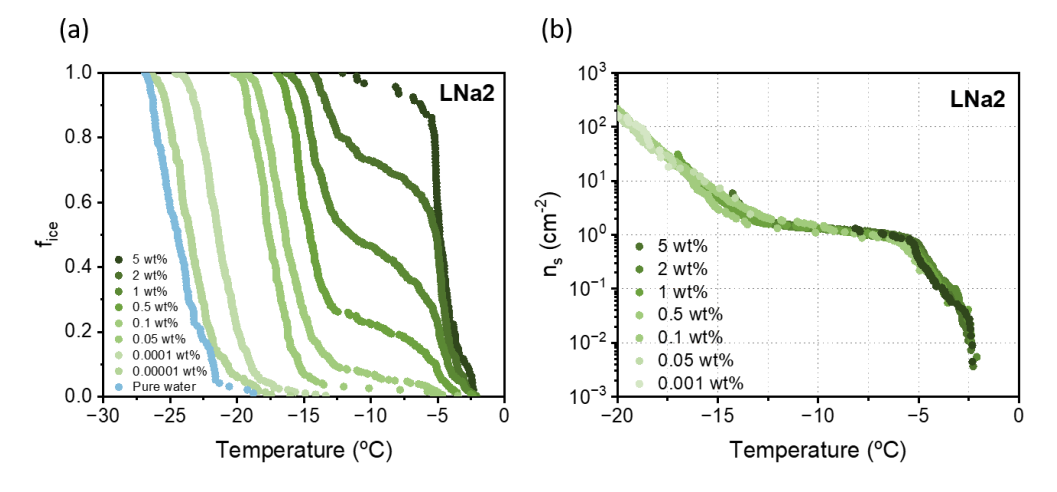


Table 2. BET analysis of the powder for each sample ($m^2 g^{-1}$) and particle size (μm) according to laser diffraction. D90, D50, D10, and average values are provided. *Notice that for LNa2, two different powder sizes were studied.

Samples		BET Surface area (m ² g ⁻¹)	D10 (μm)	D50 (μm)	D90 (μm)	Average (μm)
IK1		2.69	2.5	5.3	10.3	5.9
IK2		1.74	2.5	9.0	28.7	12.7
LNaK1		1.43	3.0	9.5	27.1	12.6
LNaK2		5.29	0.5	2.7	12.0	4.4
LNa1		1.35	3.9	16.0	38.1	19.0
LNa2*	LNa2 'large'	1.37	4.0	16.1	37.3	18.8
	LNa2 'small'	5.43	0.2	3.6	13.9	5.4

215 3.3 Fraction of frozen droplets and cumulative surface-site density

Figure 3a depicts the fraction of frozen droplets, $f_{ice}(T)$, for LNa2 feldspar (Na-rich) suspensions for a wide range of concentrations. At the highest concentration (5 wt%), nearly 90% of the droplets froze once the temperature reached approximately -4 °C. As the concentration decreased, freezing shifted to lower temperatures; at 0.1 wt%, 90% of the droplets remained unfrozen until the temperature dropped below -20 °C. At the lowest concentrations (≤ 0.01 wt%), the freezing behavior becomes indistinguishable from that of water. Each $f_{ice}(T)$ curve in Fig. 3a represents data from 192 to 288 droplets (2–3 replicates of 96-droplet arrays). Across the entire series of concentrations tested, between 1,500 and 2,500 freezing events were recorded per feldspar powder, providing a statistically robust dataset for characterizing the mineral's IN activity. The complete set of $f_{ice}(T)$ for all samples is shown in Fig. S4 in the supplementary material. The freezing behavior $f_{ice}(T)$ was further recorded over three successive freeze-thaw cycles of the same droplet arrays to assess the stability of the samples under repeated freezing. The results showed no significant differences in $f_{ice}(T)$, confirming the stability of the nucleation behavior (see Fig. S5 in the supplementary material). Although the low LOI values indicate that no substantial organic content is present in the feldspar samples, selected samples were also tested for $f_{ice}(T)$ after heating at 90 °C and 110 °C for 30 min. Again, no differences were observed, suggesting that biological contamination is unlikely to contribute to ice nucleation in our samples.





245



Figure 3. a) Fraction of frozen droplets, $f_{ice}(T)$, as a function of temperature for LNa2 feldspar suspensions at eight different concentrations (5 to 0.001 wt%). Freezing of purified water is also shown. b) Cumulative active-site density, $N_s(T)$, derived from the $f_{ice}(T)$ data using Eq. (1) normalized to sample area for LNa2.

To further evaluate the IN behavior of feldspar powders, the cumulative freezing spectrum of each mineral was derived based on Vali's methodology (Vali, 1971). This approach assumes that each individual INP has a characteristic freezing temperature that is independent of its thermal history. Within each droplet, the INP with the highest nucleation temperature governs the freezing event. Given an initial number of droplets, N_0 , and the number of frozen droplets, $N_F(T)$, the cumulative number of active INPs $N_m(T)$ can be calculated as in Eq. (1) (de Almeida Ribeiro et al., 2023; Vali, 1971, 2019).

240
$$N_{\rm m}(T) = \frac{1}{x} [\ln N_0 - \ln N_{\rm F}(T)] = \frac{1}{x} \ln[1 - f_{\rm ice}(T)]$$
 (1)

where $N_L(T) = N_0 - N_F(T)$ is the number of unfrozen droplets at temperature T, and X is a normalization factor (e.g., per unit mass, volume, or surface area of the INPs). For mineral dust, X is often taken as the ice-nucleating surface area available per droplet ($X = S_a$), which yields the cumulative active-site density per unit area, denoted as $N_s(T)$. In Fig. 3b, the $N_s(T)$ spectrum is shown, obtained from Eq. (1), and normalized to the specific surface area of the powders, which was determined using the BET method. Notably, the contributions to this spectrum obtained from different concentrations overlap well within the temperature range where each concentration exhibits high freezing activity, indicating that the relative distribution of icenucleating sites remains unaffected by dilution. These spectra serve as a quantitative measure for comparing the IN efficiency among different feldspar samples.

250 Figure 4 compares the cumulative active-site density spectra of feldspars grouped by composition: Figure 4a compares K-rich samples (IK1, IK2), Fig. 4b shows Na-rich samples (LNa1, LNa2), and Fig. 4c includes feldspars with balanced K/Na composition (LNaK1, LNaK2). Figure 4d contrasts representative spectra from each compositional group: IK1 (highest K content), LNa1 (highest Na content), and LNaK1 (lacking a clear dominance of either K or Na), allowing for a direct comparison of IN efficiencies.



260

265



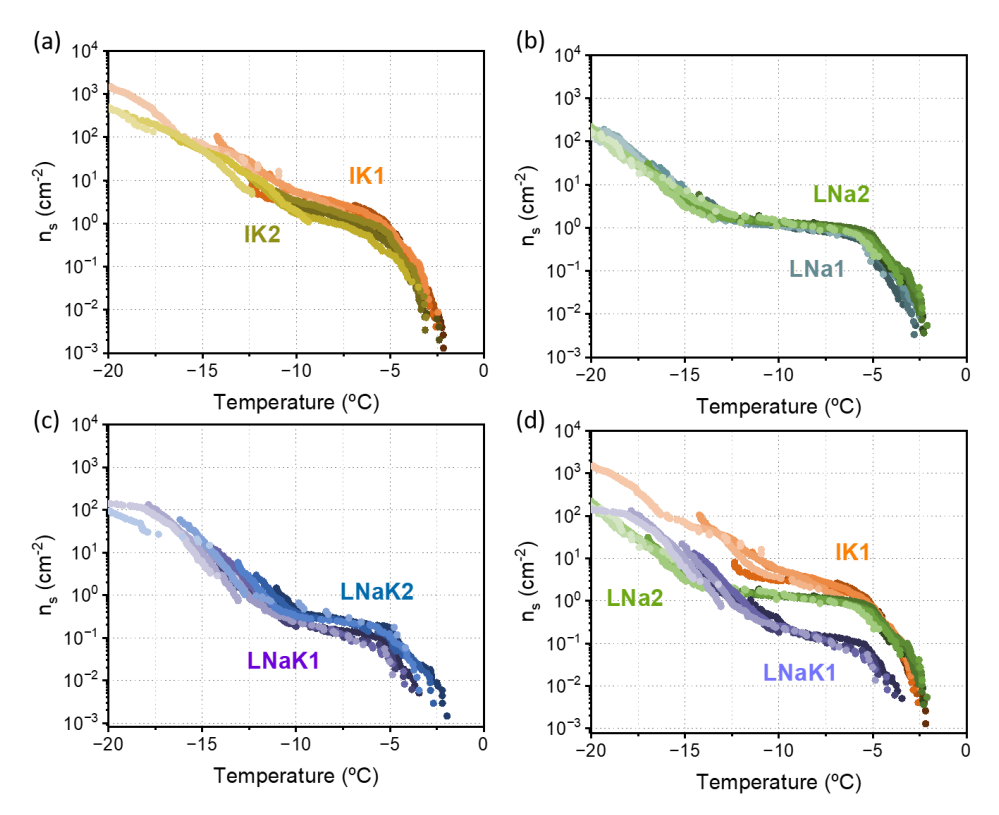


Figure 4. Cumulative active-site density freezing spectra, $N_s(T)$, obtained from $f_{ice}(T)$, normalized by specific area (in cm⁻²) as calculated using Eq. (1). a) K-rich feldspars (IK1, IK2) from Imerys b) Na-rich feldspars (LNa1, LNa2) from LLANSÀ S.A. c) Feldspars with approximately balanced K/Na composition (LNaK1, LNaK2) from LLANSÀ S.A. d) Comparison of representative samples from each feldspar type: IK1 (highest K content), LNa1 (highest Na content), and LNaK1 (no clear dominance of K or Na).

3.4. Powder size effect on the Cumulative number of Ice nucleators

LNa2 powder was ground to obtain two particle-size fractions, referred to as 'small-particles' and 'large-particles', with specific surface areas of 5.43 and 1.37 m² g⁻¹, respectively (see Table 2). Figure 5 illustrates the corresponding cumulative freezing spectra normalized to mass (Fig. 5a) and to specific surface area (Fig. 5b). When normalized by mass, the finer particles display higher $N_{\rm m}(T)$, an effect arising from their greater surface area per unit mass rather than from intrinsically enhanced activity. Upon normalization to surface area, the spectra converge to nearly identical $N_{\rm s}(T)$, indicating that icenucleating efficiency is governed by the mineral surface itself and is independent of particle size, for the sizes studied here.





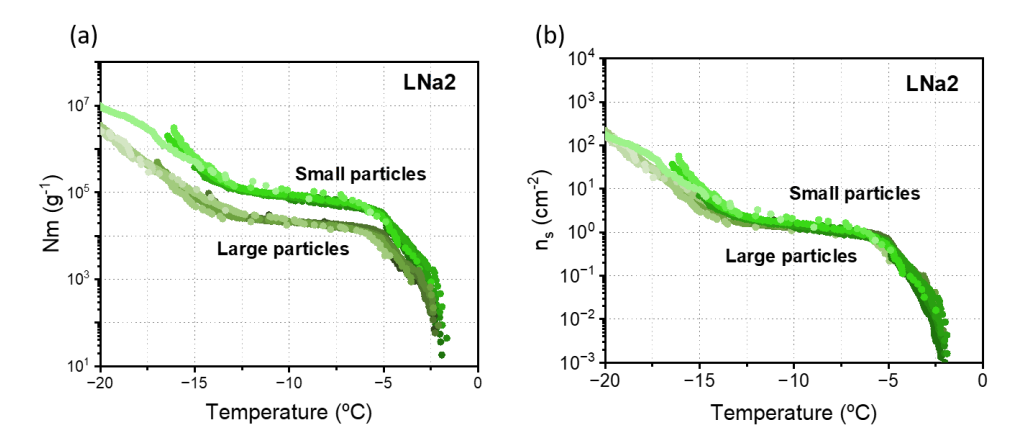


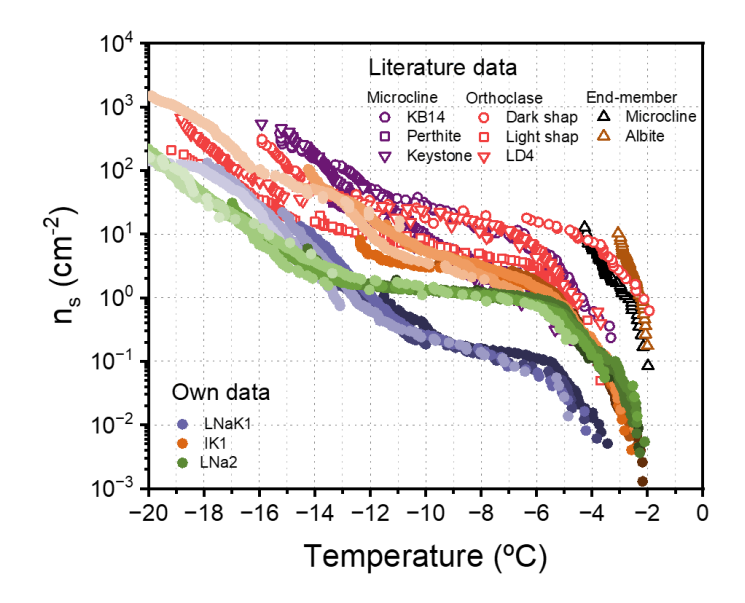
Figure 5. Cumulative freezing spectra of LNa2 powder, derived from $f_{ice}(T)$ and calculated using Eq. (1), which was ground into two particle-size fractions referred to as 'small particles' and 'large particles', with specific surface areas of 5.43 and 1.37 m² g⁻¹, respectively (see Table 2). The spectra are normalized with respect to a) the mass of feldspar powder, and b) the specific surface area.





275 4. Discussion

The results presented in this study are consistent with previously reported cumulative active-site density freezing spectra, $N_s(T)$, for perthitic feldspars. In Fig. 6, representative $N_s(T)$ spectra from each feldspar type analyzed in this study are compared with literature data for perthitic feldspars (Whale et al., 2017), along with two additional feldspars showing very high IN activity which are considered nearly pure Mc and Ab (Harrison et al., 2016).



280

Figure 6. Cumulative active-site density, $N_s(T)$, freezing spectra for selected feldspars from this study: IK (K-rich), LNa (Narich), and LNaK (intermediate), plotted alongside literature data: perthitic alkali feldspars from Whale et al. (2017) (Microcline: KB14, Perthite, Keystone; Orthoclase: Dark Shap, Light Shap, LD4) - and from Harrison et al. (2016) - nearly pure Microcline and Albite.

285

290

A key observation — both in this study and in previous literature— is the consistent onset of freezing within a narrow temperature range, approximately between -2 and -4 °C. This range is clearly observed in our data, most likely due to the relatively high feldspar concentrations used (2, 5, and 10 wt%), which enables a precise determination of initial freezing temperatures. In fact, onset temperatures remain remarkably similar across all tested samples. Averaging values for the first 10 freezing events ($T_{(i,10)}$) for each sample fall within this narrow range: $T_{(i,10)}(IK1) = -2.3$ °C, $T_{(i,10)}(IK2) = -2.5$ °C, $T_{(i,10)}(IK3) = -2.3$ °C, $T_{(i,10)}(IK3) = -2.3$ °C. In contrast, many previously published studies report slightly lower onset temperatures, as shown in Fig. 6 (Harrison et al., 2016; Whale et al., 2017). It is important to note that those studies used lower concentrations of feldspar (typically ≤ 1 wt%) compared to the concentrations used in our experiments. This lower concentration can make it more difficult to detect onset temperatures



310

315

320

325



295 triggered by IN sites with low population densities. At higher concentrations, these sites would be expected to trigger freezing within the −2 to −4 °C range observed here. In the case of Ab and Mc, which show exceptionally high IN efficiency, the steep slope (nearly vertical) of their freezing spectra at higher temperatures suggests that increasing the concentration would not significantly shift the onset temperature upward. This narrow range highlights the uniformity of active sites across feldspar types, supporting the hypothesis that a shared nucleation mechanism is operative. Conversely, for other feldspar types reported in the literature—such as Pl, which show much lower onset temperatures—it is unlikely that increased concentrations would bring their initial freezing into the same range observed for alkali feldspars. These observations suggest that the most active nucleation sites in alkali feldspars are likely shared across all samples, resulting in a common onset temperature. Therefore, the differences in the cumulative spectra (Fig. 5) are best interpreted as a reflection of the density of these active sites (denoted as *N*_s(*T*), the number of sites per cm², as well as the presence and abundance of other, less active site populations that contribute to nucleation at lower temperatures.

As shown in Fig. 4, powders originating from the same mine and exhibiting similar mineralogy and K/Na ratios display nearly identical cumulative freezing spectra within the statistical uncertainty of the measurements. For example, IK1 and IK2 exhibit analogous trends in freezing behavior and site densities (Fig. 4a), although IK1 displays a slightly higher density down to approximately $-15\,^{\circ}$ C, where deviations become more pronounced. It should be noted that although both powders, IK1 and IK2, come from different fronts of the same mine, the lack of precise spatial coordinates limits the extent to which site-specific variability can be assessed.

In contrast, feldspars from the Llançà mine were collected with more precise location data, enabling a more detailed assessment of the geological influence on IN properties. Minerals were collected from three distinct fronts, each separated by more than 500 m. These fronts exhibit compositional variability in terms of K/Na content: one dominated by Na-rich feldspar, another by K-rich feldspar, and a third characterized by more heterogeneous Na/K content. Feldspars LNa1 and LNa2, sourced from the Na-rich and the compositionally variable front, respectively, exhibit nearly identical freezing spectra (Fig. 4b), as well as similar K/Na ratios and mineralogical characteristics (Table 3). Despite originating from different extraction fronts, the close similarity of their ice-nucleating behavior suggests that both samples likely formed under comparable geological conditions, resulting in analogous surface properties that govern IN activity. A similar pattern is observed between LNaK1 and LNaK2, sourced from the Na-rich and K-rich fronts, respectively. Although LNaK1 exhibits a slightly higher K/Na ratio, it shows a lower density of nucleation sites down to -15 °C (Fig. 4c). Despite this, both samples maintain a comparable spectral shape, supporting the idea that macroscopically consistent mineralogical properties translate into predictable IN behavior, even when minor compositional differences exist.

The consistency of these results is further supported by the observation that, within the particle size fraction used in this study, powder preparation from bulk rock appears to have minimal impact on IN efficiency. We compared powders of the same mineral ground to different particle sizes (Fig. 5). At equal mass concentrations, finer powder induces more freezing events per temperature interval, reflecting higher $N_{\rm m}(T)$ due to greater surface exposure. Nevertheless, after normalizing by BET-



350



derived S_a , the freezing behavior converged across all particle sizes, indicating that IN activity is primarily governed by intrinsic surface chemistry and structural properties rather than by particle size or preparation method itself.

A previous study (Welti et al., 2019)(8) reported a correlation between particle size and IN activity, yet the effect was limited to particles < 1 μm, which are significantly smaller than those examined here. The same study further suggested that the Rb/Sr ratio may serve as a predictor of the expected freezing temperatures, with higher ratios linked to greater nucleation efficiency. Our data corroborate this: IK1 and IK2 show Rb/Sr ratios nearly an order of magnitude higher than the other powders (see Table S2 in the supplementary material) and correspondingly display higher IN sites densities between −5 to −20 °C.

To further explore differences in freezing spectra across feldspars with varying Na/K ratio, the distribution of heterogeneous nucleation temperatures was analyzed using the Heterogeneous Underlying-Based (HUB) method (de Almeida Ribeiro et al., 2023; Renzer et al., 2024). This approach employs a stochastic optimization algorithm to fit the experimental cumulative spectra with a linear combination of Gaussian subpopulations, each representing a distinct class of IN sites. The resulting differential spectra resolve the distribution of nucleation temperatures, thereby enabling characterization of the underlying subpopulations.

Figure 7a shows the cumulative freezing for LNa1, with the optimized HUB fit (in red), assuming the differential spectrum consists of a linear combination of three Gaussian subpopulations (Fig. 7b). Figure 7c displays the corresponding normalized distribution function, $n_{\rm m}(T)$, representing the differential freezing spectrum. A mean squared error (MSE) below or approximately 0.01 was achieved when a linear combination of three distinct subpopulations was included in the fitting. Fitting the spectra with two subpopulations, corresponding to two distinct IN classes, failed to reproduce the initial freezing behavior of feldspar powders, yielding an MSE of 0.0652. A more accurate solution is achieved by considering three subpopulations, which lowers MSE to 0.0041 (see Fig. S6 and Table S4 in the supplementary material).

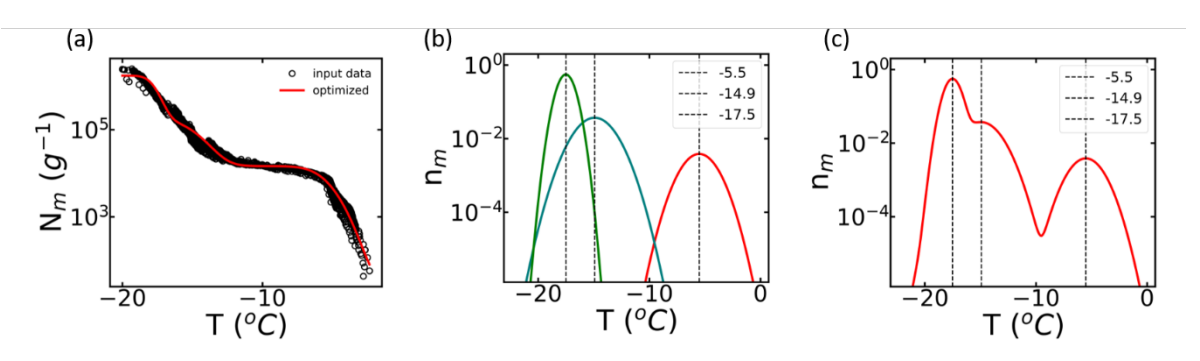


Figure 7. a) Cumulative freezing spectra of LNa1. The red line corresponds to the optimized solution obtained through the HUB method, assuming that the differential spectrum is a linear combination of three Gaussian IN subpopulations shown in b). c) Normalized distribution function that represents the corresponding differential freezing spectra $n_{\rm m}(T)$.

Throughout the analysis, we compare $n_{\rm m}(T)$ of alkali feldspars by grouping them according to their K/Na ratio: K-rich (IK), intermediate (LNaK), and Na-rich (LNa). Figure 8 displays the differential freezing spectra from all analyzed samples,





segmented into three temperature-defined regions: A (0 to -7.5 °C), B (-7.5 to -12.5 °C) and C (-12.5 to -20 °C). Correspondingly, Table S3 summarizes, for all analyzed feldspars, the temperatures corresponding to the subpopulations of the differential freezing spectra, the associated freezing probability within these ranges and MSE.

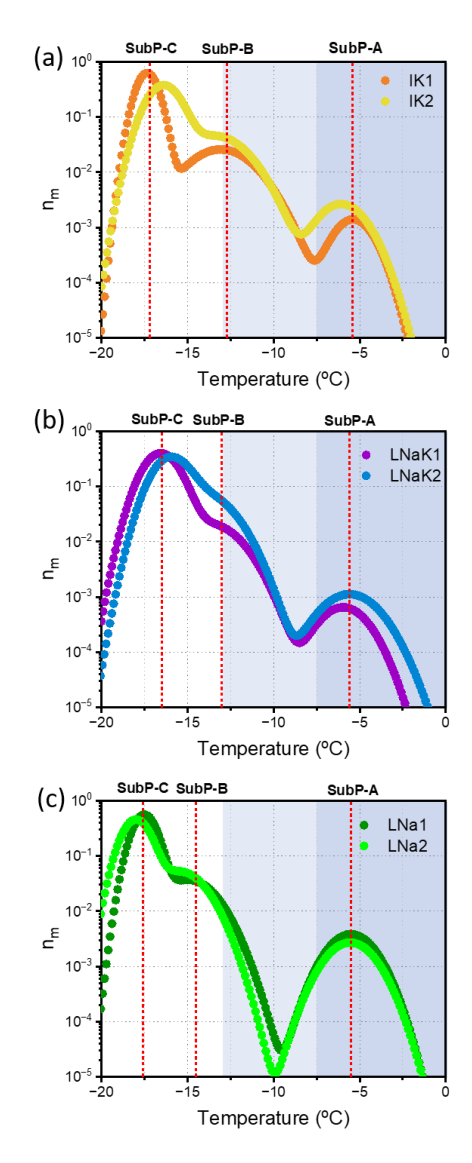


Figure 8. Normalized distribution function that represents the corresponding differential freezing spectra $n_{\rm m}(T)$ of feldspar powders obtained with the HUB method (de Almeida Ribeiro et al., 2023). Vertical red dashed lines indicate the temperature ranges associated with distinct subpopulations of ice-nucleating sites (SubP-A, SubP-B, and SubP-C). a) K-rich feldspars (IK1 and IK2), b) feldspars with similar K/Na ratio (LNaK1 and LNaK2), and c) Na-rich feldspars (LNa1 and LNa2).





Several trends emerge from the analysis presented in Fig. 8 and Table S3. First, the initial IN active population (SubP-A) does not exhibit a clear difference between Na-rich (anti-perthitic) and K-rich (perthitic) feldspars, as both groups initiate freezing at very similar temperatures. The probability of freezing associated with the first subpopulation appears to be higher in IK samples. In contrast, the second IN population (SubP-B) displays an inverse trend: IK feldspars nucleate at slightly higher freezing temperatures on average (≈ -13.3 to -13.5 °C) than LNa samples (≈ -13.3 and -15.2 °C). Notably, between -7 °C and -13 °C, LNa samples, corresponding to an anti-perthitic Or structure, show very low IN activity, with no subpopulation peak assigned to this temperature region, leading to an extended plateau in their $N_s(T)$ cumulative spectra, as observed in Fig. 4d. Feldspars with a similar Na to K ratio, i.e., LNaK samples, exhibit spectra between those of the IK samples and LNa samples (Fig. 4b).

To contextualize these findings within existing literature, a HUB analysis was performed on published cumulative freezing data from Whale et al. (2017) for six perthitic feldspars (Fig. 9, and their fitted parameters are summarized in Table S5 of the Supplementary material). Feldspars in Fig. 9a are predominantly composed of Or, while those in Fig. 9b are primarily Mc, both being polymorphs of K-feldspar. Only datasets with high point density and confirmed perthitic microstructures were selected: Light Shap (K/Na = 2.3, Or), Dark Shap (K/Na = 2.3, Or), LD4 (K/Na unknown, Or), Perthite (K/Na = 1.3, Mc), KB14 (K/Na = 0.67, Mc) and Keystone (K/Na = 4, Mc) (Whale et al., 2017). As illustrated by the cumulative $N_s(T)$ freezing spectra in Fig. 6, these feldspars exhibit contrasting freezing behaviors: Or-feldspars display flat regions (red curves), while Mc show a more gradual and continuous increase in activity with decreasing temperature (purple curves). The HUB analysis of these six feldspars, presented in Fig. 9, identifies three distinct nucleating populations, in line with the three regions also identified in our feldspar powders in Fig. 8.



390

395

400



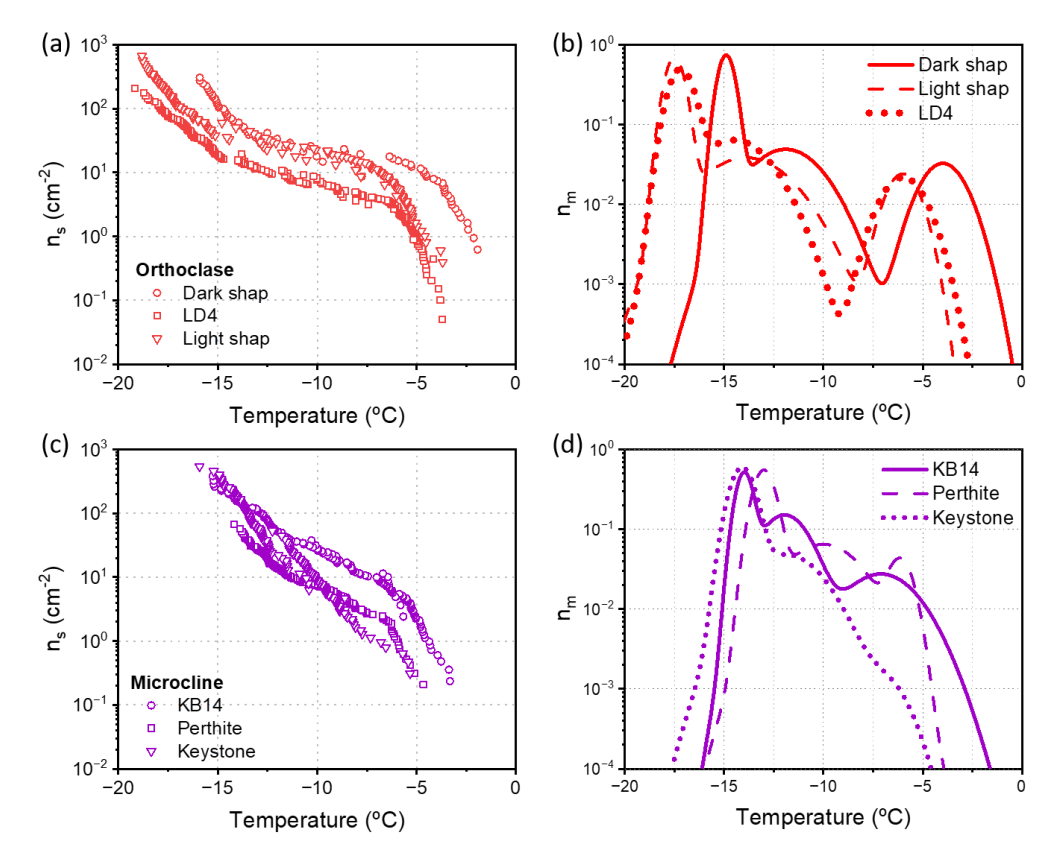


Figure 9. Cumulative ice-nucleating site densities, $N_s(T)$, and corresponding normalized differential spectra, $n_{\rm m}(T)$, using the HUB method (de Almeida Ribeiro et al., 2023) from selected data of perthites published by Whale et al. (2017) a-b) Orthoclase perthites (Dark Shap, Light Shap and LD4), c-d) Microcline perthites (KB14, Perthite, Keystone).

Published data (Welti et al., 2019) show that the two groups of perthitic feldspars (Mc and Or) do not systematically differ in their K/Na ratios; rather, the primary distinction appears to lie in their mineralogical composition. The samples with a plateau in their cumulative $N_s(T)$ freezing spectra are characterized by two main subpopulations at high temperatures: one active at higher temperatures, and a second that becomes active at significantly lower temperatures. A third subpopulation is also needed for a correct fitting at temperatures below -15 °C. The two main subpopulations are separated by a temperature range where no active population is observed. In contrast, the samples without a plateau show a more gradual and continuous activation of populations with decreasing temperature. Interestingly, similar trends have been observed in this study (Welti et al., 2019), where Or tends to show an initial activity followed by a plateau, while Mc exhibits a steady increase in activity. However, due to limitations in the available data, a HUB analysis could not be performed on those additional samples. It is widely accepted that, based on published data, at a given temperature, Mc tends to be generally more active in enhancing ice nucleation than



405

410

415

420

425



other K-feldspar polymorphs (Augustin-Bauditz et al., 2014; Welti et al., 2019), a behavior attributed to its higher degree of structural ordering.

Crystallographic surface ordering has been shown to play a key role in heterogeneous nucleation efficiency (Sosso et al., 2022). In feldspars, ice preferentially nucleates on the (100) crystallographic face. While this does not involve perfect epitaxial matching, similar alignment has been proposed as a contributing factor in other materials (Shimizu et al., 2018; Verdaguer et al., 2006). Nevertheless, SEM observations of feldspars have revealed preferential ice growth depending on crystallographic orientation of the substrate, suggesting partial structural matching between the ice and feldspar surface (A. Kiselev et al., 2016; Pach & Verdaguer, 2019). This effect is believed to be primarily driven by the arrangement of hydroxyl (OH) groups on the mineral surface (Franceschi et al., 2024; A. Kiselev et al., 2016; Pedevilla et al., 2016). Molecular dynamics simulations further support this interpretation, suggesting that the density of OH groups plays a more critical role in governing IN activity than lattice symmetry (Pedevilla et al., 2017). Experimental studies have further demonstrated that chemical modification of the OH group density can significantly impact the ice-nucleating ability of feldspar surface (A. Kiselev et al., 2016; Pach & Verdaguer, 2021; Peckhaus et al., 2016). Our analysis suggests that the first subpopulation, characterized by a Gaussian distribution centered between -5 and -6 °C, does not appear to be strongly influenced by either the Na/K ratio or the specific K-feldspar polymorph (Mc or Or). However, the density of this subpopulation appears to be higher in both K-rich and Na-rich perthite feldspars compared to those with more balanced Na/K ratios. This pattern suggests that the nucleation activity in this temperature range may not be directly governed by the degree of crystallographic ordering within the feldspar, but rather by structural imperfections or defects. These defects are likely associated with the exsolution textures typical of perthitic structures. This interpretation is supported by observations of Pl-feldspars, which lack such perthitic textures and only exhibit ice nucleation at significantly lower temperatures. In contrast, the progressive increase in nucleation activity at lower temperatures appears to correlate more closely with the presence of Mc. In samples where Mc is not the predominant phase, no new subpopulations are detected even after additional cooling of nearly -10 °C. This trend is evident in both Or-dominated samples from the literature (Fig. 9a) and in the Na-rich feldspars analyzed in this study, which contain only minor amounts of Mc (LNa) (Fig. 8c). At temperatures below ca. −15 °C, additional subpopulations consistently emerge across all examined feldspar samples, indicating a general transition to a different nucleation regime.





Conclusions

430

435

440

445

450

455

Ice nucleation (IN) properties of K and Na feldspars with perthitic textures were investigated under immersion freezing conditions. Six samples, collected from two different mines and five distinct extraction fronts, were analyzed. Freezing activity was systematically characterized through experiments using a wide range of suspensions with varying particle concentrations. For each sample, more than 1,000 freezing events were evaluated, enabling the generation of robust and statistically meaningful cumulative freezing spectra. While the density of active ice-nucleating sites varied significantly between samples, the initial freezing onset temperatures were remarkably consistent and closely aligned with values reported in previous studies. This shared onset behavior is likely characteristic of perthitic feldspars, given that other feldspar types, such as Pl, tend to activate at lower temperatures. Samples with similar mineralogical compositions and microstructures exhibited nearly identical freezing spectra, supporting the idea that ice nucleation efficiency is governed primarily by intrinsic material properties rather than by sampling location.

Two distinct nucleation behaviors were identified. One group of samples displayed a pronounced plateau following the initial freezing onset, indicating a lack of new active site formation until further cooling triggered a second increase in activity. The other group showed a continuous increase in IN site density following onset, with no evident plateau. Notably, these two patterns are not exclusive to the samples studied here; similar behaviors are also observed in previously published freezing spectra, suggesting that they represent generalizable nucleation modes for feldspars.

To better resolve the nature of the underlying ice-nucleating sites, the HUB method was employed to deconvolute the cumulative spectra into Gaussian subpopulations. This analysis revealed a fundamental difference between the two nucleation behaviors: plateau-containing spectra are consistent with two well-separated subpopulations—one initiating near onset and another emerging at lower temperatures—whereas continuous spectra require multiple, more gradually activated subpopulations.

A comparison with published mineralogical data suggests that these behaviors are linked to the crystallographic nature of the K-feldspar phase. Samples showing no additional subpopulations after onset often contain more disordered orthoclase, whereas those with continuous activity tend to be associated with the more ordered Mc polymorph. These observations support the hypothesis that the initial onset of freezing is driven by defects related to perthitic intergrowths, while the development of additional IN populations at lower temperatures is influenced by the degree of structural ordering within the feldspar.

Given the importance of feldspar in atmospheric ice nucleation—particularly in the formation of mixed-phase clouds (Atkinson et al., 2013; Chatziparaschos et al., 2023), that affect climate feedbacks (B. J. Murray et al., 2021), —these findings have implications for improving the accuracy of cloud microphysics in climate models (Burrows et al., 2022). Beyond atmospheric science, the ability of feldspar to nucleate ice at relatively high temperatures also holds potential for various technological applications that require enhanced ice formation, such as cryopreservation (Daily et al., 2023; K. A. Murray & Gibson, 2022). A deeper understanding and identification of mineralogical features that promote IN, along with locating reliable natural sources of such materials may therefore offer both scientific and technological value.



465

470

480



460 Data availability. Additional characterization is provided in the Supplementary Information, and the dataset is available at https://doi.org/10.5281/zenodo.17396669 (Canet et., al 2025).

Authors contributions. AV and LR designed and conceptualized the study. JC and GR conducted the research under supervision of AV, KM and MB. AV led the original draft preparation and were completed by JC, LR, and MGV. GR, KM and MB reviewed the writing, JC and AV analysed and interpreted the data. KM and GR contributed to the interpretation of the results. MGV and PA performed characterization, analysis and provided expertise into the mineralogical aspects. JC and MGV prepared the visualization.

Competing interests. The authors declare that they have no conflict of interest.

Acknowledgements. We thank the Spanish Ministry of Science and Innovation (MCIN) and State Investigation Agency (AEI) under projects TED2021-129572B-I00, CPP2021-009093 and PID2023-153245NB-I00 and through the Severo Ochoa Programme for Centres of Excellence in R&D (CEX2023-001263-S) for supporting this work. We would like to express our gratitude to the help of Albert Orue from Feldespatos Llansa SA, and Michel Galvin, for providing us with feldspar samples.

475 We acknowledge the contribution from ICMAB-CSIC's Scientific & Technological Services, in particular Dr. Alejandro Borràs, for performing the BET measurements. We acknowledge the assistance of Dr. Janine Fröhlich-Nowoisky and Dr. Anna-Lena Leifke for their laboratory support at Max Planck Institute for Chemistry, JC acknowledges the financial support mobility grant iMOVE2024 (IMOVE24165) and I-Link (ILINK24045) from the Spanish Ministry of Science and Innovation. This work has been performed in the framework of the Ph.D. program "Chemistry and Chemical Engineering" of IQS by JC.

Financial support. This research was funded by the Spanish Ministry of Science and Innovation (MCIN) and State Investigation Agency (AEI) under projects TED2021-129572B-I00, CPP2021-009093 and PID2023-153245NB-I00 and through the Severo Ochoa Programme for Centres of Excellence in R&D (CEX2023-001263-S). I-Link project (ILINK24045) was funded by the Spanish Ministry of Science and Innovation. JC received financial support from the Spanish Ministry of

485 Science and Innovation under the mobility grant iMOVE2024 (IMOVE24165).





References

505

515

- Atkinson, J. D., Murray, B. J., Woodhouse, M. T., Whale, T. F., Baustian, K. J., Carslaw, K. S., Dobbie, S., O'Sullivan, D., & Malkin, T. L.: The importance of feldspar for ice nucleation by mineral dust in mixed-phase clouds. Nature, 498(7454), 355–358. https://doi.org/10.1038/nature12278, 2013.
 - Augustin-Bauditz, S., Wex, H., Kanter, S., Ebert, M., Niedermeier, D., Stolz, F., Prager, A., & Stratmann, F.: The immersion mode ice nucleation behavior of mineral dusts: A comparison of different pure and surface modified dusts. Geophysical Research Letters, 41(20), 7375–7382. https://doi.org/10.1002/2014GL061317, 2014.
- 495 Canet, J., Rodríguez, L., Renzer, G., Alfonso, P., Bonn, M., Meister, K., Garcia-Valles, M., Verdaguer, A.: [data set], https://doi.org/10.5281/zenodo.17396669, 2025.
 - Brunauer, S., Emmett, P. H., & Teller, E.: Adsorption of Gases in Multimolecular Layers. Journal of the American Chemical Society, 60(2), 309–319. https://doi.org/10.1021/ja01269a023, 1938.
- Burrows, S. M., McCluskey, C. S., Cornwell, G., Steinke, I., Zhang, K., Zhao, B., Zawadowicz, M., Raman, A., Kulkarni, G.,
 China, S., Zelenyuk, A., & DeMott, P. J.: Ice-Nucleating Particles That Impact Clouds and Climate: Observational and
 Modeling Research Needs. In Reviews of Geophysics (Vol. 60, Issue 2). John Wiley and Sons Inc.
 https://doi.org/10.1029/2021RG000745, 2022.
 - Chatziparaschos, M., Daskalakis, N., Myriokefalitakis, S., Kalivitis, N., Nenes, A., Goncalves Ageitos, M., Costa-Suros, M., Perez Garcia-Pando, C., Zanoli, M., Vrekoussis, M., & Kanakidou, M.: Role of K-feldspar and quartz in global ice nucleation by mineral dust in mixed-phase clouds. Atmospheric Chemistry and Physics, 23(3), 1785–1801. https://doi.org/10.5194/acp-23-1785-2023, 2023.
 - Cziczo, D. J., Froyd, K. D., Hoose, C., Jensen, E. J., Diao, M., Zondlo, M. A., Smith, J. B., Twohy, C. H., & Murphy, D. M.: Clarifying the Dominant Sources and Mechanisms of Cirrus Cloud Formation. Science, 340(6138), 1320–1324. https://doi.org/10.1126/science.1234145, 2013.
- Daily, M. I., Whale, T. F., Kilbride, P., Lamb, S., John Morris, G., Picton, H. M., & Murray, B. J.: A highly active mineral-based ice nucleating agent supports in situ cell cryopreservation in a high throughput format. Journal of the Royal Society Interface, 20(199). https://doi.org/10.1098/rsif.2022.0682, 2023.
 - de Almeida Ribeiro, I., Meister, K., & Molinero, V.: HUB: a method to model and extract the distribution of ice nucleation temperatures from drop-freezing experiments. Atmospheric Chemistry and Physics, 23(10), 5623–5639. https://doi.org/10.5194/acp-23-5623-2023, 2023.
 - Franceschi, G., Conti, A., Lezuo, L., Abart, R., Mittendorfer, F., Schmid, M., & Diebold, U.: How Water Binds to Microcline Feldspar (001). Journal of Physical Chemistry Letters, 15(1), 15–22. https://doi.org/10.1021/acs.jpclett.3c03235, 2024.
 - Friddle, R. W., & Thürmer, K.: How nanoscale surface steps promote ice growth on feldspar: microscopy observation of morphology-enhanced condensation and freezing. 11(44), 21147–21154. https://doi.org/10.1039/c9nr08729j, 2019.



540



- Harrison, A. D., Whale, T. F., Carpenter, M. A., Holden, M. A., Neve, L., O'Sullivan, D., Vergara Temprado, J., & Murray, B. J.: Not all feldspars are equal: A survey of ice nucleating properties across the feldspar group of minerals. In Atmospheric Chemistry and Physics (Vol. 16, Issue 17, pp. 10927–10940). Copernicus GmbH. https://doi.org/10.5194/acp-16-10927-2016, 2016.
- Hoose, C., & Möhler, O.: Heterogeneous ice nucleation on atmospheric aerosols: A review of results from laboratory experiments. In Atmospheric Chemistry and Physics (Vol. 12, Issue 20, pp. 9817–9854). https://doi.org/10.5194/acp-12-9817-2012, 2012.
 - Kanji, Z. A., Ladino, L. A., Wex, H., Boose, Y., Burkert-Kohn, M., Cziczo, D. J., & Krämer, M.: Overview of Ice Nucleating Particles. Meteorological Monographs, 58, 1.1-1.33. https://doi.org/10.1175/amsmonographs-d-16-0006.1, 2017.
- Kiselev, A. A., Keinert, A., Gaedeke, T., Leisner, T., Sutter, C., Petrishcheva, E., & Abart, R.: Effect of chemically induced fracturing on the ice nucleation activity of alkali feldspar. Atmospheric Chemistry and Physics, 21(15), 11801–11814. https://doi.org/10.5194/acp-21-11801-2021, 2021.
 - Kiselev, A., Bachmann, F., Pedevilla, P., Cox, S. J., Michaelides, A., Gerthsen, D., & Leisner, T.: Active sites in heterogeneous ice nucleation-the example of K-rich feldspars. Science, 355(6323), 367–371. https://doi.org/10.1126/science.aai8034, 2016.
- 535 Knopf, D. A., & Alpert, P. A.: Atmospheric ice nucleation. Nature Reviews Physics, 5(4), 203–217. https://doi.org/10.1038/s42254-023-00570-7, 2023.
 - Kunert, A. T., Lamneck, M., Helleis, F., Pöschl, U., Pöhlker, M. L., & Fröhlich-Nowoisky, J.: Twin-plate Ice Nucleation Assay (TINA) with infrared detection for high-Throughput droplet freezing experiments with biological ice nuclei in laboratory and field samples. Atmospheric Measurement Techniques, 11(11), 6327. https://doi.org/10.5194/amt-11-6327-2018, 2018.
 - Liang, M., Cheng, Y., Zhou, X., Liu, J., & Wang, J.: Determining Roles of Potassium-Feldspar Surface Characters in Affecting Ice Nucleation. Small Methods, 8(4). https://doi.org/10.1002/smtd.202300407, 2024.
 - Murray, B. J., Carslaw, K. S., & Field, P. R.: Opinion: Cloud-phase climate feedback and the importance of ice-nucleating particles. Atmospheric Chemistry and Physics, 21(2), 665–679. https://doi.org/10.5194/acp-21-665-2021, 2021.
- Murray, B. J., O'sullivan, D., Atkinson, J. D., & Webb, M. E.: Ice nucleation by particles immersed in supercooled cloud droplets. Chemical Society Reviews, 41(19), 6519–6554. https://doi.org/10.1039/c2cs35200a, 2012.
 - Murray, K. A., & Gibson, M. I.: Chemical approaches to cryopreservation. Nature Reviews Chemistry, 6(8), 579–593. https://doi.org/10.1038/s41570-022-00407-4, 2022.
- Pach, E., & Verdaguer, A.: Pores Dominate Ice Nucleation on Feldspars. Journal of Physical Chemistry C, 123(34), 20998–21004. https://doi.org/10.1021/acs.jpcc.9b05845, 2019.
 - Pach, E., & Verdaguer, A.: Freezing efficiency of feldspars is affected by their history of previous freeze-thaw events. Physical Chemistry Chemical Physics, 23(43), 24905–24914. https://doi.org/10.1039/d1cp02548a, 2021.



555



- Peckhaus, A., Kiselev, A., Hiron, T., Ebert, M., & Leisner, T.: A comparative study of K-rich and Na/Ca-rich feldspar ice-nucleating particles in a nanoliter droplet freezing assay. Atmospheric Chemistry and Physics, 16(18), 11477–11496. https://doi.org/10.5194/acp-16-11477-2016, 2016.
- Pedevilla, P., Cox, S. J., Slater, B., & Michaelides, A.: Can Ice-Like Structures Form on Non-Ice-Like Substrates? The Example of the K-feldspar Microcline. Journal of Physical Chemistry C, 120(12), 6704–6713. https://doi.org/10.1021/acs.jpcc.6b01155, 2016.
- Pedevilla, P., Fitzner, M., & Michaelides, A.: What makes a good descriptor for heterogeneous ice nucleation on OH-patterned surfaces. Physical Review B, 96(11). https://doi.org/10.1103/PhysRevB.96.115441, 2017.
 - Renzer, G., de Almeida Ribeiro, I., Guo, H. B., Fröhlich-Nowoisky, J., Berry, R. J., Bonn, M., Molinero, V., & Meister, K.: Hierarchical assembly and environmental enhancement of bacterial ice nucleators. Proceedings of the National Academy of Sciences of the United States of America, 121(43). https://doi.org/10.1073/pnas.2409283121, 2024.
- Shimizu, T. K., Maier, S., Verdaguer, A., Velasco-Velez, J. J., & Salmeron, M.: Water at surfaces and interfaces: From molecules to ice and bulk liquid. In Progress in Surface Science (Vol. 93, Issue 4, pp. 87–107). Elsevier Ltd. https://doi.org/10.1016/j.progsurf.2018.09.004, 2018.
 - Sosso, G. C., Sudera, P., Backes, A. T., Whale, T. F., Fröhlich-Nowoisky, J., Bonn, M., Michaelides, A., & Backus, E. H. G.: The role of structural order in heterogeneous ice nucleation. Chemical Science, 13(17). https://doi.org/10.1039/d1sc06338c, 2022.
- Vali, G.: Quantitative evaluation of experimental results on the heterogeneous freezing nucleation of supercooled liquids.

 Journal of the Atmospheric Sciences, 28(3), 402–409. https://doi.org/10.1175/1520-0469(1971)028<0402:QEOERA>2.0.CO;2, 1971.
 - Vali, G.: Interpretation of freezing nucleation experiments: Singular and stochastic; Sites and surfaces. Atmospheric Chemistry and Physics, 14(11), 5271–5294. https://doi.org/10.5194/acp-14-5271-2014, 2014.
- Vali, G.: Revisiting the differential freezing nucleus spectra derived from drop-freezing experiments: Methods of calculation, applications, and confidence limits. Atmospheric Measurement Techniques, 12(2), 1219–1231. https://doi.org/10.5194/amt-12-1219-2019, 2019.
 - Verdaguer, A., Sacha, G. M., Bluhm, H., & Salmeron, M.: Molecular structure of water at interfaces: Wetting at the nanometer scale. In Chemical Reviews (Vol. 106, Issue 4, pp. 1478–1510). https://doi.org/10.1021/cr0403761, 2006.
- Welti, A., Lohmann, U., & Kanji, Z. A.: Ice nucleation properties of K-feldspar polymorphs and plagioclase feldspars. Atmospheric Chemistry and Physics, 19(16), 10901–10918. https://doi.org/10.5194/acp-19-10901-2019, 2019.
 - Whale, T. F., Holden, M. A., Kulak, A. N., Kim, Y. Y., Meldrum, F. C., Christenson, H. K., & Murray, B. J.: The role of phase separation and related topography in the exceptional ice-nucleating ability of alkali feldspars. Physical Chemistry Chemical Physics, 19(46), 31186–31193. https://doi.org/10.1039/c7cp04898j, 2017.